The Astrophysical Journal, 933:5 (15pp), 2022 July 1 https://doi.org/10.3847/1538-4357/ac6fce

Modeling the Optical to Ultraviolet Polarimetric Variability from Thomson Scattering in Colliding-wind Binaries

Richard Ignace[1], Andrew Fullard[2], Manisha Shrestha[3], Yaël Nazé[4,9], Kenneth Gayley[5], Jennifer L. Hoffman[6], Jamie R. Lomax[7], and Nicole St-Louis[8]
[1] Department of Physics & Astronomy, East Tennessee State University, Johnson City, TN 37614, USA; ignace@etsu.edu
[2] Department of Physics and Astronomy, Michigan State University, East Lansing, MI 48824, USA
[3] Astrophysics Research Institute, Liverpool John Moores University, Liverpool Science Park, 146 Brownlow Hill, Liverpool L3 5RF, UK
[4] GAPHE, UR STAR, Université de Liège, Allée du 6 Août 19c (B5C), B-4000 Sart Tilman, Liège, Belgium
[5] Department of Physics & Astronomy, University of Iowa, Iowa City, IA 52242, USA
[6] Department of Physics & Astronomy, University of Denver, 2112 E. Wesley Ave., Denver, CO 80208, USA
[7] Department of Physics, United States Naval Academy, 572C Holloway Rd., Annapolis, MD 21402, USA
[8] Département de physique, Université de Montréal, Complexe des Sciences, 1375 Avenue Thérèse-Lavoie-Roux, Montréal (Qc), H2V 0B3, Canada
Received 2022 February 24; revised 2022 May 2; accepted 2022 May 13; published 2022 June 28

Abstract

Massive-star binaries are critical laboratories for measuring masses and stellar wind mass-loss rates. A major challenge is inferring viewing inclination and extracting information about the colliding-wind interaction (CWI) region. Polarimetric variability from electron scattering in the highly ionized winds provides important diagnostic information about system geometry. We combine for the first time the well-known generalized treatment of Brown et al. for variable polarization from binaries with the semianalytic solution for the geometry and surface density CWI shock interface between the winds based on Cantó et al. Our calculations include some simplifications in the form of inverse-square law wind densities and the assumption of axisymmetry, but in so doing they arrive at several robust conclusions. One is that when the winds are nearly equal (e.g., O+O binaries) the polarization has a relatively mild decline with binary separation. Another is that despite Thomson scattering being a gray opacity, the continuum polarization can show chromatic effects at ultraviolet wavelengths but will be mostly constant at longer wavelengths. Finally, when one wind dominates the other, as, for example, in WR+OB binaries, the polarization is expected to be larger at wavelengths where the OB component is more luminous and generally smaller at wavelengths where the WR component is more luminous. This behavior arises because, from the perspective of the WR star, the distortion of the scattering envelope from spherical is a minor perturbation situated far from the WR star. By contrast, the polarization contribution from the OB star is dominated by the geometry of the CWI shock.

Unified Astronomy Thesaurus concepts: Spectropolarimetry (1973); Stellar winds (1636); Massive stars (732)

1. Introduction

Despite composing the rarest stellar mass group, massive stars ($>8\,M_{\odot}$) are the most important originators of elements in the universe because they synthesize and distribute heavy elements when they explode as supernovae (Nomoto et al. 2013). Massive stars also enrich the interstellar medium during their presupernova lifetime via their strong stellar winds. High levels of mass loss also affect the evolution of massive stars, in particular the nature of their remnants (Puls et al. 2008; Langer 2012; Smith 2014).

Most massive stars spend a large fraction of their lives in binary systems with other massive stars; approximately 50% are thought to engage in mass exchange with a close companion (Sana et al. 2012). Interactions between companions drive the evolutionary paths that can shape both stars' subsequent fates (e.g., Langer 2012; Song et al. 2016).

Colliding-wind binaries can teach us a great deal about the individual stars and their winds because the geometry of the interaction region is dependent on the relative mass-loss rates and velocities of the binary components. Early theories describing these binaries used momentum flux (e.g., Girard & Willson 1987) and ram pressure balance (e.g., Kallrath 1991), or hydrodynamic models (e.g., Stevens et al. 1992), and even some semianalytic work (e.g., Usov 1992; Cantó et al. 1996; Pilyugin & Usov 2007; Gayley 2009). Further work in the area has focused on hydrodynamic simulations (Parkin & Pittard 2008; Lamberts et al. 2011; MacLeod & Loeb 2020) and predictions of line profiles in both optical (Luehrs 1997; Georgiev & Koenigsberger 2004; Ignace et al. 2009) and X-rays (Henley et al. 2003; Rauw et al. 2016; Mossoux & Rauw 2021). The result of these models, combined with a number of phase-resolved observations, is that we have generally a good understanding of the expected geometry of colliding winds (e.g., Rauw et al. 1999; Gosset et al. 2001; Sana et al. 2004; Gosset et al. 2009; Williams et al. 2009; Kennedy et al. 2010; Fahed et al. 2011; Nazé et al. 2012; Cazorla et al. 2014; Rauw et al. 2014; Lomax et al. 2015; Gosset & Nazé 2016; Nazé et al. 2018; Callingham et al. 2020; Rodríguez et al. 2020).

Given that massive-star winds are strongly ionized, it is natural to consider Thomson scattering as the dominant scattering opacity in the winds, which in turn can polarize the observed light. The resulting polarization is sensitive to the geometry of the scattering regions. The classic (Brown et al. 1978, hereafter BME) model approximates the time-varying continuum polarization caused by the illumination of

[9] FNRS Senior Research associate.

circumstellar material in a binary system viewed at an arbitrary inclination angle. Those authors assume that the electron scattering region is optically thin. Their approach allows for a general geometry, but for binary stars they consider two point sources of illumination and a corotating scattering envelope.

Brown et al. (1982) extended the BME model to consider elliptical orbits, and Fox (1994) further extended the formalism to consider finite-size illuminators. Fox (1994) showed that occultation is only important in very close binary systems, where the separation of stars is less than 10 times the radius of the primary. However, none of these enhancements to the theory specifically addressed the effects of colliding winds in the time-dependent polarization results. Furthermore, the effects of the wind collision regions on the wavelength dependence of polarization have not been considered as part of this theoretical framework. However, such polarized signals associated with colliding winds have been observed in several systems (St.-Louis et al. 1993; Lomax et al. 2015). A modeling effort in this domain is therefore critically important.

Polarization models of stellar wind bow shock structures produced by the interaction of stellar winds with a local ambient medium shows that significant polarization can arise from scattering of light in these structures (Shrestha et al. 2018, 2021). Modeling the polarization signal caused by colliding-wind geometries has been done specifically for the system V444 Cyg (St.-Louis et al. 1993; Kurosawa et al. 2002), but a general formalism has not yet been produced. In this paper we derive a consistent model for the polarization signal produced by wind collision regions in massive binary systems. In Section 2 we describe our model of polarimetric variability from optically thin electron scattering in a shock illuminated by two stars. In Section 3 we derive expressions for the polarization signal based on the system parameters and show how these expressions lead to chromatic and orbital effects in polarization. We summarize our results in Section 4.

2. Polarimetric Variability from Thin Electron Scattering

Our treatment is based on that of BME, who presented a thorough theoretical construction for thin electron scattering in a generalized envelope with an arbitrary number of illuminating point sources. With regard to our application for a binary system, we assume that the colliding-wind interaction (CWI) is axisymmetric about the line of centers (LOC) joining the two stars (i.e., we ignore the Coriolis effect in our example cases, though this has been detected in at least one colliding-wind binary; Lomax et al. 2015). We further assume that the separate winds of the two stars are each spherically symmetric up to the CWI. As a result, in the notation of BME, we have $\gamma_1 = \gamma_2 = \gamma_3 = \gamma_4 = 0$, and the only factors that are nonzero are γ_0 and τ_0. In our development we will modify this notation slightly.

BME then considered the more limited scenario of a binary system with a circular orbit and corotating envelope. Our approach allows for elliptical orbits (which Brown et al. 1982 later considered), and for the shape and density of the bow shock, we employ the analytical solution of Cantó et al. (1996).

The Cantó et al. (1996) solution is predicated on strong radiative cooling. There are two initial concerns about adopting this model. The first is that radiative cooling leads to thin-shell instabilities (e.g., Lamberts et al. 2011). The second is that radiative cooling is limited to relatively close binaries, orbital periods of order a week (e.g., Antokhin et al. 2004). These issues have significant relevance for predicting X-ray spectra, where the temperature distribution along the shock is important, or when simulating emission-line profile shapes, where the detailed vector velocity field is crucial. However, our case deals with electron scattering and continuum polarization. Unlike the case of X-ray diagnostics, where the distribution of hot gas is important, we can safely assume that the gas is everywhere highly ionized for computing scattering polarization. Of chief importance to our case is that the Cantó et al. (1996) derivation is conveniently analytic and driven by considerations of ram pressure balance, which captures much of the key physics. Most, but not all, of our examples involve either equal winds or binaries with one dominant wind, and our general conclusions based on the Cantó et al. (1996) model are fairly robust.

As in the BME formalism, our approach assumes point-source illumination. This is reasonable when the binary separation is not too small (of order the stellar radii). One distinction, however, is that we do account for finite stellar size when evaluating volume integrals. This is not incompatible with BME; we are merely explicit about its inclusion.

A final point about our use of the BME treatment is that, due to the axisymmetry, we employ the notation and approach of BME for a single star and use superposition in our application to a binary system. In doing so, our notation departs from BME, although we still employ similar variables. The following sections introduce our geometry for the systems, our application of BME to axisymmetric binaries, and semianalytic solutions for the variable polarization based on the Cantó et al. (1996) solution for the CWI.

2.1. Geometry and Stellar Properties

In our model, the winds of the two stars and the intervening colliding-wind shock are prescribed using primarily polar coordinates for each star. We define the primary star to be the one with the stronger wind in terms of momentum flux, $\dot{M}v_\infty$, where $\dot{M}$ is the mass-loss rate and v_∞ is the terminal wind speed. The secondary is then the weaker wind case in terms of this product. We typically use subscripts "1" and "2" to identify primary and secondary.

We introduce spherical coordinates with respect to the axis that is the LOC between the two stars. Coordinates centered on the primary star (r_1, θ_1, ϕ_1) are such that $\theta_1 = 0$ in the direction of the secondary. Likewise, the coordinates linked to the secondary star (r_2, θ_2, ϕ_2) also have $\theta_2 = 0$ in the direction of the primary. Frequently, our approach employs the standard cosine notation, $\mu_1 = \cos\theta_1$ and $\mu_2 = \cos\theta_2$.

The individual winds are taken to be spherical, with densities varying with the inverse square of the distance from the star. Consequently, we are ignoring the wind acceleration zone that is relevant whenever the bow shock forms close to either or both stars. We do not include the potential for radiative braking of the stronger wind if it enters the region of dominance of the companion stellar flux (Gayley et al. 1997; Lomax et al. 2015), nor the possibility that the stronger wind might in some cases ram directly into the photosphere of the secondary star.

With spherical winds and constant speed radial outflow, the density relations for the primary and secondary winds are

$$\rho_1 = \frac{\dot{M}_1}{4\pi\, r_1^2\, v_1} = \rho_{1,0}\left(\frac{R_{1,*}}{r_1}\right)^2, \quad (1)$$

$$\rho_2 = \frac{\dot{M}_2}{4\pi\, r_2^2\, v_2} = \rho_{2,0}\left(\frac{R_{2,*}}{r_2}\right)^2, \text{ and} \tag{2}$$

$$n_1 = n_{1,0}\left(\frac{R_{1,*}}{r_1}\right)^2, \tag{3}$$

$$n_2 = n_{2,0}\left(\frac{R_{2,*}}{r_2}\right)^2, \tag{4}$$

where n_j for $j = 1,\ 2$ are electron number densities with corresponding scale parameter $n_{j,0} = \rho_0/\mu_e m_H$, with m_H the mass of hydrogen and μ_e the mean molecular weight per free electron. Since we consider terminal speed flow, we have omitted the subscript ∞ for the primary and secondary wind speeds in Equations (1) and (2).

2.2. Bow Shock Model

To explore polarimetric variability from colliding-wind shocks, we choose the formulation of Cantó et al. (1996) for their semianalytic bow shock solution involving radiative cooling and two stellar spherical winds at terminal speed. This solution specifically assumes radiative cooling, and the bow shock takes the form of an interface of infinitesimal thickness between the two otherwise spherical winds. This interface for the CWI is axisymmetric and characterized with a surface density.

Here we reproduce in brief the key expressions for the solution of Cantó et al. (1996), but with a few changes of notation. Cantó et al. (1996) use a "1" subscript for the primary but no subscript for the secondary; we use a "2" subscript for the secondary. Cantó et al. (1996) use σ for the surface mass density, while we use $\Sigma = \sigma/\mu_e m_H$ for the surface number density of electrons. In principle μ_e is a function of position in either wind and in the bow shock itself; however, for simplicity, we assume that μ_e is constant throughout the shock.

The bow shock geometry and its surface density are related to two fundamental ratios:

$$\beta = \frac{\dot{M}_2 v_2}{\dot{M}_1 v_1}, \tag{5}$$

$$\alpha = v_2/v_1. \tag{6}$$

The first of these, $\beta \leqslant 1$, is the ratio of wind momentum of the secondary compared to the primary; the second, α, is the ratio of wind terminal speeds. Figure 1 provides a schematic of the binary system with intervening CWI region between the two stars. The radial distances of the bow shock from the stars are denoted as $R_{1,S}$ and $R_{2,S}$, with

$$R_{2,S} = D\,\frac{\sin\theta_1}{\sin(\theta_1+\theta_2)}, \tag{7}$$

$$R_{1,S} = \sqrt{D^2 + R_{2,S}^2 - 2\,D\,R_{2,S}\cos\theta_1}, \tag{8}$$

where D is the separation between the two stars at any moment. We denote the standoff radii of the bow shock from each star along the LOC as $R_{1,0}$ and $R_{2,0}$, with

$$R_{2,0} = \frac{\beta^{1/2}}{1-\beta^{1/2}}\,D, \tag{9}$$

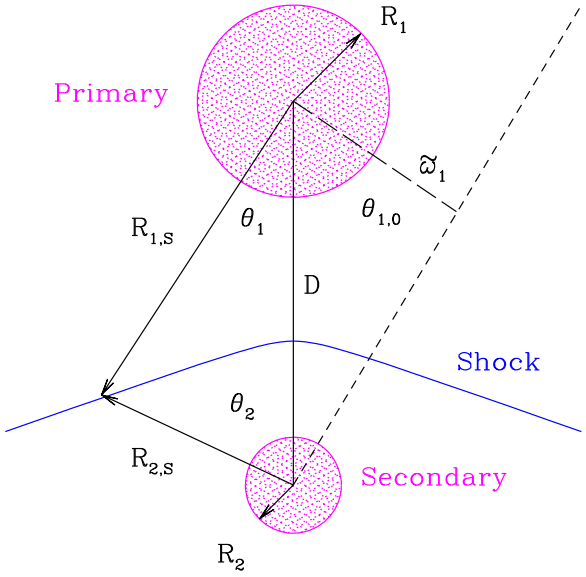

Figure 1. Top-down illustration of the two stars, primary and secondary, in magenta and the bow shock in blue, formed by the colliding winds. Labeled variables are defined in text.

$$R_{1,0} = \frac{1}{1-\beta^{1/2}}\,D. \tag{10}$$

While the above relations are analytic formulations in θ_1 and θ_2, the relation between the two coordinate angles is implicit, making the solution overall semianalytic. The relationship of the angles is given by

$$\frac{\theta_1}{\tan\theta_1} = 1 + \beta\left(\frac{\theta_2}{\tan\theta_2} - 1\right). \tag{11}$$

Note that the asymptotic angles ("opening angles") for the bow shock are given by

$$\theta_{2,\infty} - \tan\theta_{2,\infty} = \frac{\pi}{1-\beta}, \tag{12}$$

$$\theta_{1,\infty} = \pi - \theta_{2,\infty}. \tag{13}$$

The case $\beta = 1$ corresponds to a planar shock between identical stars and winds, with $\theta_{1,\infty} = \theta_{2,\infty} = \pi/2$.

The final key ingredient for modeling the polarimetric variability is the surface number density distribution. Again from Cantó et al. (1996), this is given by

$$\begin{aligned}\frac{\Sigma}{\Sigma_0} = &\frac{\sin(\theta_1+\theta_2)}{\sin\theta_1\sin\theta_2} \\ &\times [\beta(1-\cos\theta_2) + \alpha(1-\cos\theta_1)]^2 \\ &\times \{[\beta(\theta_2 - \sin\theta_2\cos\theta_2 + (\theta_1 - \sin\theta_1\sin\theta_2)]^2 \\ &+ (\beta\sin^2\theta_2 - \sin^2\theta_1)^2\}^{-1/2},\end{aligned} \tag{14}$$

where the scaling constant is

$$\begin{aligned}\Sigma_0 &= \frac{\dot{M}_2/\mu_e m_H}{2\pi\beta\, D\, v_2} = \frac{2R_{2,*}}{\beta\, D}\,R_{2,*}n_{2,0} \\ &= \alpha\,\frac{2R_{1,*}}{D}\,R_{1,*}n_{1,0}.\end{aligned} \tag{15}$$

The last step in the above expression represents the surface number density as being twice the column depth of the wind of the secondary from the bow shock to infinity.

In the special case of $\beta = 1$ for a planar shock forming from two identical stars, $R_{1,S} = R_{2,S} = D/2\mu$, where $\mu = \cos\theta$ with $\theta = \theta_1 = \theta_2$. Combined with $\alpha = 1$, the surface density then simplifies to

$$\frac{\Sigma}{\Sigma_0} = 4\,\frac{\cos\theta(1 - \cos\theta)^2}{\sin\theta(\theta - \sin\theta\cos\theta)}. \tag{16}$$

Having defined the geometry of the CWI interface and its properties, we turn next to characterizing the electron scattering polarization.

2.3. Thin Scattering

As previously noted, we employ the approach of BME in application to the results of Cantó et al. (1996), which is explicitly axisymmetric. In the treatment of BME, ignoring absorption and assuming that the total amount of scattered light is small compared to the specific luminosities of either star, the polarization is given by

$$p_{\rm tot} = \tau(1\text{–}3\gamma)\sin^2 i = p_0\,\sin^2 i, \tag{17}$$

where $p_{\rm tot}$ is the polarization, τ is an angle-averaged optical depth of the envelope, γ is called the shape factor, and i is the viewing inclination relative to the symmetry axis of the envelope. We introduce p_0 for conveniently representing the product of optical depth and envelope shape. The definitions of τ and γ are

$$\tau = \frac{3}{16}\sigma_{\rm T}\int\!\!\int n(r,\,\mu)dr\,d\mu \tag{18}$$

and

$$\gamma = \frac{\int\!\!\int n(r,\,\mu)dr\,\mu^2\,d\mu}{\int\!\!\int n(r,\,\mu)\,dr\,d\mu}, \tag{19}$$

where $n(r,\,\mu)$ is the axisymmetric distribution of electrons throughout the scattering volume. If the scattering region is spherically symmetric, $\gamma = 1/3$, and the polarization is zero. For a wind whose density varies as the inverse of the squared distance, $\tau = 3\tau_*/8$, with $\tau_* = n_0\,\sigma_{\rm T}\,R_*$ being the radial optical depth of the wind in electron scattering.

The integrals for τ and γ are defined with respect to the star center, and the treatment for axisymmetry does not require top-down symmetry. Thus, one can introduce τ_1 and γ_1 associated with polarization from scattering of starlight from the primary, and then τ_2 and γ_2 for scattering of starlight by the secondary. Being optically thin, the results add linearly as weighted by the wavelength-dependent luminosities of the two stars:

$$p_0 = \frac{L_1(\lambda)p_1 + L_2(\lambda)p_2}{L_1(\lambda) + L_2(\lambda)}. \tag{20}$$

This result, in our notation, is equivalent to Equations (6a) and (7) from BME for axisymmetry. The dependence on viewing inclination is implicit in Equation (20) via Equation (17). As pointed out by BME, we have that $i_1 = i_2 = i$ so that $p_{\rm tot} = p_0\,\sin^2 i$ as in Equation (17) earlier.

Note that for a particular geometry as expressed by the wind and orbital properties, p_1 and p_2 have generally different values but are defined with respect to the same axis, the LOC between the stars. While these values are not wavelength dependent (i.e., chromatic), p_0 can be chromatic because the two illuminating sources will generally have different spectral energy distributions (SEDs).

This last point deserves additional comment. When one star dominates the brightness of the system in a given wavelength range, the polarization will be flat and take the polarization value of the dominant star. At wavelengths for which the emission of both stars follows a Rayleigh–Jeans law, the relative contribution to the total luminosity of the stars will always be the same; hence, $p_{\rm tot}$ will also be flat. However, for stars of unequal temperatures, at wavelengths around the Wien peak, the ratio of specific luminosities will vary, and either p_1 or p_2 may dominate, or the dominant terms may switch. Thus, for hot stars, p_0 will be chromatic at short wavelengths, despite the fact that electron scattering is gray.

3. Model Results

3.1. Expressions for the Polarization

Recall that for BME the polarization depends on source parameters τ and γ, but these in turn depend on angle-averaged column densities of free electrons. It is convenient to introduce two varieties of angle-averaged column densities, one that is a zeroth-order moment and one that is a second-order moment:

$$\langle N\rangle = \frac{1}{2}\int\!\!\int n(r,\,\mu)dr\,d\mu \tag{21}$$

and

$$\langle \tilde{N}\rangle = \frac{1}{2}\int\!\!\int n(r,\,\mu)dr\,\mu^2\,d\mu. \tag{22}$$

Then,

$$\tau = \frac{3}{8}\sigma_{\rm T}\left\langle N\right\rangle \tag{23}$$

and

$$\gamma = \langle\tilde{N}\rangle/\langle N\rangle, \tag{24}$$

where these parameters would have subscript 1 or 2 for the primary or secondary stars, respectively. For example, the primary wind with density given by Equation (3) would have a first-moment column density of $\langle N_1\rangle = n_{1,0}R_{1,*}$.

In application to the colliding-wind binary, there are three key angular regimes to consider in relation to each of the two stars. These three solid angle sectors contribute to the parameters $\gamma_{1,2}$ and $\tau_{1,2}$. These will be detailed next in terms of Cases A, B, and C, with reference to Figure 2.

Figure 2 is a copy of Figure 1 in terms of the stars and the CWI (labeled as "Shock"), now used to emphasize the three angular regimes. There is still the LOC with separation D. Using the secondary as an example, three rays are labeled with A2, B2, and C2. Similar rays could be drawn as originating from the primary, which would then be labeled A1, B1, and C1. Consequently,

$$\langle N\rangle = \langle N_A\rangle + \langle N_B\rangle + \langle N_C\rangle \tag{25}$$

and

$$\langle\widetilde{N}\rangle = \langle\widetilde{N_A}\rangle + \langle\widetilde{N_B}\rangle + \langle\widetilde{N_C}\rangle. \tag{26}$$

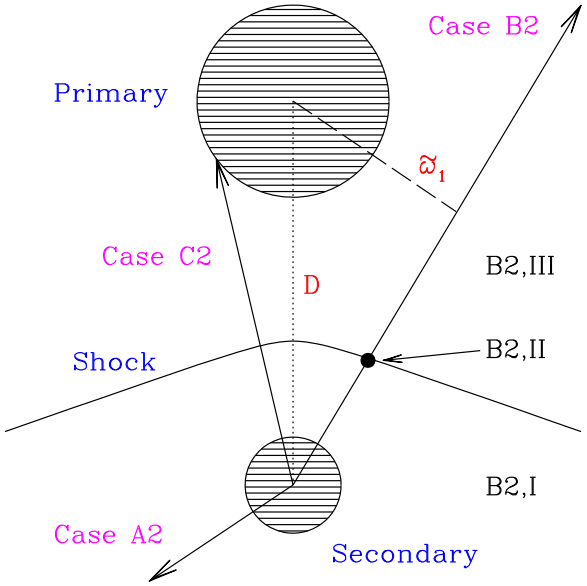

Figure 2. Similar to Figure 1, the two stars and colliding-wind shock are illustrated. For calculation of the polarization properties, column density moments involve three different ray categories, here identified as A2, B2, and C2 in relation to the secondary star. The dotted line is the LOC for separation D between the stars. The impact parameter ϖ_1 is the same as for Figure 1. For Case B2, the contributions associated with I (path segment), II (point), and III (semi-bound line segment) are identified.

3.1.1. Case A: Rays Not Intersecting the Colliding-wind Shock

For $\theta_1 > \theta_{1,\infty}$ or $\theta_2 > \theta_{2,\infty}$, the ray does not intersect the shock or the opposite star but travels strictly through its own wind. In this case the angle-averaged column densities are trivial for an inverse-square law, with

$$\langle N_{A1}\rangle = \frac{1}{2} n_{1,0} R_{1,*}(1 + \mu_{1,\infty}), \tag{27}$$

$$\langle \tilde{N}_{A1}\rangle = \frac{1}{6} n_{1,0} R_{1,*}(1 + \mu_{1,\infty}^3), \tag{28}$$

$$\langle N_{A2}\rangle = \frac{1}{2} n_{2,0} R_{2,*}(1 + \mu_{2,\infty}), \tag{29}$$

$$\langle \tilde{N}_{A2}\rangle = \frac{1}{6} n_{2,0} R_{2,*}(1 + \mu_{2,\infty}^3). \tag{30}$$

3.1.2. Case B: Rays Intersecting the Shock but Not the Opposite Star

When a ray intersects the shock, there are three distinct contributions to the relevant angle-averaged column densities: a segment of the star's own wind, the surface density at the shock itself, and finally a segment through the wind of the opposite star. The ray does not intercept the surface of the opposite star, a case treated in the next section.

We denote these three contributions as I for the star's own wind, II for the shock, and III for the opposite wind, and we use these as subscripts to accompany 1 and 2 to signify whether the rays originate from the primary or the secondary star. Note that the angular integrations are affected by the ray missing or intercepting the opposite star.

The first segment is the column within the star's own wind from its surface to the shock. The columns are

$$\langle N_{B1,I}\rangle = \frac{1}{2} n_{1,0} R_{1,*} \int_{\mu_{1,\infty}}^{\mu_{2,*}} \left[1 - \frac{R_{1,*}}{R_{1,S}(\mu)}\right] d\mu, \tag{31}$$

$$\langle N_{B2,I}\rangle = \frac{1}{2} n_{2,0} R_{2,*} \int_{\mu_{2,\infty}}^{\mu_{1,*}} \left[1 - \frac{R_{2,*}}{R_{2,S}(\mu)}\right] d\mu, \tag{32}$$

$$\langle \tilde{N}_{B1,I}\rangle = \frac{1}{2} n_{1,0} R_{1,*} \int_{\mu_{1,\infty}}^{\mu_{2,*}} \left[1 - \frac{R_{1,*}}{R_{1,S}(\mu)}\right] \mu^2\, d\mu, \tag{33}$$

$$\langle \tilde{N}_{B2,I}\rangle = \frac{1}{2} n_{2,0} R_{2,*} \int_{\mu_{2,\infty}}^{\mu_{1,*}} \left[1 - \frac{R_{2,*}}{R_{2,S}(\mu)}\right] \mu^2\, d\mu, \tag{34}$$

where $\mu_{1,*} = \cos\theta_{1,*} = \sqrt{1 - (R_{1,*}/D)^2}$ and $\mu_{2,*} = \cos\theta_{2,*} = \sqrt{1 - (R_{2,*}/D)^2}$. In the integrand, the fraction being subtracted represents the missing column in the star's own wind that would be present if not for the shock.

At the shock itself, the surface density contributes to the column along the ray, due to the accumulation of material entering the shock and outflowing along its surface. However, the kinematics are not of relevance here; only the surface density itself matters. What is relevant is the projection of the surface with respect to the ray. The contribution to the column depends on a direction cosine between the radial unit vector and the local normal to the surface. We represent these as $K_1(\mu)$ and $K_2(\mu)$. Omitting the subscripts, K for each star is given by

$$K(\mu) = \frac{1}{\sqrt{1 + \left(\frac{1}{R_S}\frac{dR_S}{d\theta}\right)^2}}. \tag{35}$$

Then, the contribution by the shock to the columns becomes

$$\langle N_{B1,II}\rangle = \frac{1}{2} n_{1,0} R_{1,*} \int_{\mu_{1,\infty}}^{\mu_{2,*}} K_1(\mu)\Sigma(\mu) d\mu, \tag{36}$$

$$\langle N_{B2,II}\rangle = \frac{1}{2} \int_{\mu_{2,\infty}}^{\mu_{1,*}} K_2(\mu)\Sigma(\mu) d\mu, \tag{37}$$

$$\langle \tilde{N}_{B1,II}\rangle = \frac{1}{2} \int_{\mu_{1,\infty}}^{\mu_{2,*}} K_1(\mu)\Sigma(\mu)\mu^2\, d\mu, \tag{38}$$

$$\langle \tilde{N}_{B2,II}\rangle = \frac{1}{2} \int_{\mu_{2,\infty}}^{\mu_{1,*}} K_2(\mu)\Sigma(\mu)\mu^2\, d\mu. \tag{39}$$

The third region is in the wind of the opposite star, beyond the shock. The integration in radius depends on whether the ray strikes the star or not. The former case is treated in the next section. Here we express the columns along the ray from the shock that stretches to infinity with impact parameter ϖ. Consider, for example, a ray originating from the secondary at orientation θ_2. The ray intercepts the shock at $R_{2,S}$. Further, the ray is in the wind of the primary. The impact parameter for that ray is $\varpi_1 = D\sin\theta_2$.

For a spherical wind with inverse-square density, the integration for the column along such a chord is analytic:

$$\int_{-\infty}^{z_0} n_0 \frac{R_*^2}{r^2}\, dz = n_0 R_* \frac{R_*}{\varpi(\mu)} \int_0^{\theta_0} d\theta$$
$$= n_0 R_* \frac{R_*}{\varpi(\mu)} \theta_0(\mu), \tag{40}$$

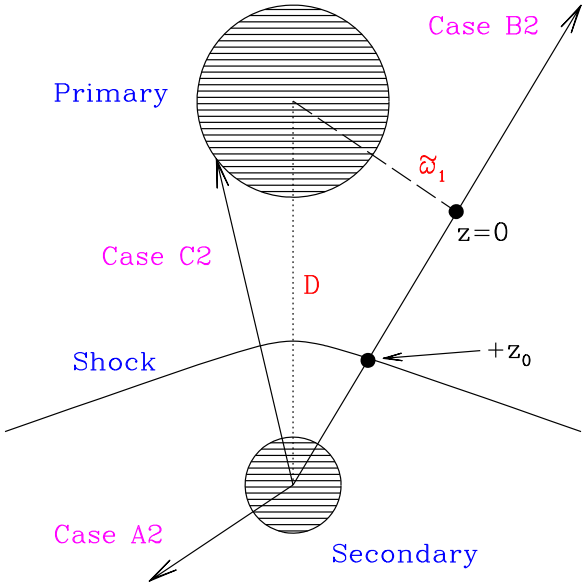

Figure 3. Similar to Figure 2, the two stars and colliding-wind shock are illustrated. Cases A2, B2, and C2 in relation to the secondary star are indicated. The z-coordinate is indicated in this version, with z_0 labeled. For columns evaluated along radials from the secondary, z is defined in the wind of the primary, and vice versa.

where the subscripts 1 and 2 have been suppressed for this general result. Take again the example of a ray from the secondary. Then, z_0 refers to the z-coordinate in the wind of the primary corresponding to $R_{1,S}$ and ϖ_1. Figure 3 shows the location of z_0 in relation to the system components. With θ_0 defined with respect to the stellar axis, one can show that $\theta_0 + \theta_1 + \theta_2 = \pi$.

The next step is to integrate in μ. Again using the secondary as an example, this integration will be of the form $\theta_0(\mu_2)d\mu_2/\varpi_1 \sim \theta_0(\theta_2)d\theta_2$. The end result from the columns for section III is

$$\langle N_{B1,III}\rangle = \frac{1}{2} n_{2,0} R_{2,*} \frac{R_{2,*}}{D} \times \int_{\theta_{1,\infty}}^{\theta_{2,*}} (\pi - \theta_1 - \theta_2) d\theta_1, \quad (41)$$

$$\langle N_{B2,III}\rangle = \frac{1}{2} n_{1,0} R_{1,*} \frac{R_{1,*}}{D} \times \int_{\theta_{2,\infty}}^{\theta_{1,*}} (\pi - \theta_1 - \theta_2) d\theta_2, \quad (42)$$

$$\langle \tilde{N}_{B1,III}\rangle = \frac{1}{2} n_{2,0} R_{2,*} \frac{R_{2,*}}{D} \times \int_{\theta_{1,\infty}}^{\theta_{2,*}} (\pi - \theta_1 - \theta_2) \cos^2\theta_1 \, d\theta_1, \quad (43)$$

$$\langle \tilde{N}_{B2,III}\rangle = \frac{1}{2} n_{1,0} R_{1,*} \frac{R_{1,*}}{D} \times \int_{\theta_{2,\infty}}^{\theta_{1,*}} (\pi - \theta_1 - \theta_2) \cos^2\theta_2 \, d\theta_2, \quad (44)$$

where $\sin\theta_{1,*} = R_{1,*}/D$ and $\sin\theta_{2,*} = R_{2,*}/D$. When the ray intercepts the opposite star, the lower limit to the integral in Equation (40) is no longer 0 in $d\theta$. Thus, the integrands for the angular integrations above are different over the solid angle extent of the opposite star.

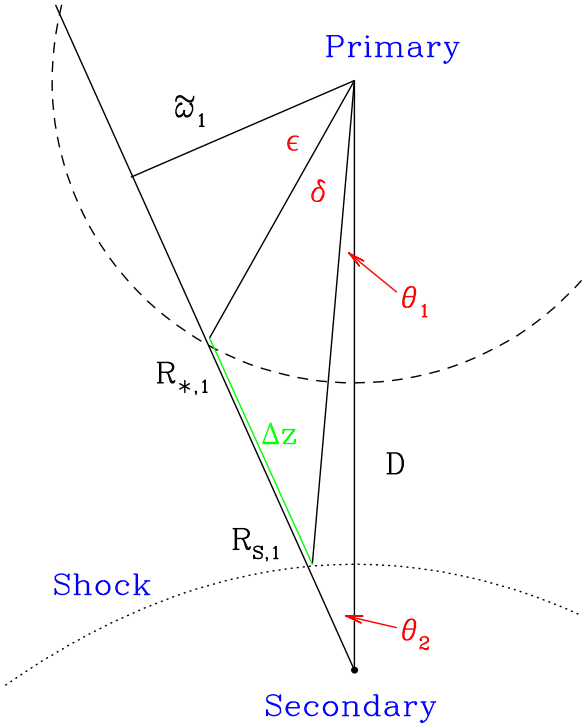

Figure 4. Similar to Figure 1, but zoomed in to emphasize angular quantities used for case C calculations. The primary star is shown at top, with its extent a dashed curve. The shock is a dotted curve. For the secondary star at bottom, only its center is indicated.

For Case B, one adds the contributions from the different segments to obtain

$$\langle N_{B1}\rangle = \langle N_{B1,I}\rangle + \langle N_{B1,II}\rangle + \langle N_{B1,III}\rangle, \quad (45)$$

$$\langle N_{B2}\rangle = \langle N_{B2,I}\rangle + \langle N_{B2,II}\rangle + \langle N_{B2,III}\rangle, \quad (46)$$

$$\langle \tilde{N}_{B1}\rangle = \langle \tilde{N}_{B1,I}\rangle + \langle \tilde{N}_{B1,II}\rangle + \langle \tilde{N}_{B1,III}\rangle, \quad (47)$$

$$\langle \tilde{N}_{B2}\rangle = \langle \tilde{N}_{B2,I}\rangle + \langle \tilde{N}_{B2,II}\rangle + \langle \tilde{N}_{B2,III}\rangle. \quad (48)$$

3.1.3. Case C: Rays That Intercept the Opposite Star

In the final scenario, case C, the ray intersects the opposite star. This modifies the upper limit for the integral associated with segment III. Segments I and II from case B are the same for case C; only segment III differs. To be explicit, for segment C,I for a star's own wind up to the shock, one still uses Equations (31)–(34) for B,I but with different limits to the integrals. The lower limit is μ_* for star 1 or 2 as appropriate, and the upper limit is $+1$ for all the integrals. Similarly, the contribution C,II at the shock uses Equations (36)–(39) for B,II also with μ_* (again, as appropriate for 1 or 2) for the lower limit and $+1$ for the upper limit. It is only C,III that requires reconsideration, as follows.

One way of expressing case C,III is that when $\varpi < R_*$, or alternatively when $\theta < \theta_*$, for the primary or secondary as the case may be, the radial integral along the chord is still given by an angle, but this angle is not θ_0. Instead, we introduce new angles ϵ and δ, with

$$\theta_1 + \theta_2 + \epsilon + \delta = \pi/2. \quad (49)$$

Figure 4 shows the locations of ϵ and δ with respect to the system. We have that $\varpi_1 = D\sin\theta_2 = R_{1,*}\cos\epsilon_1$, so that ϵ_1 is defined in terms of θ_2 for a ray originating from the

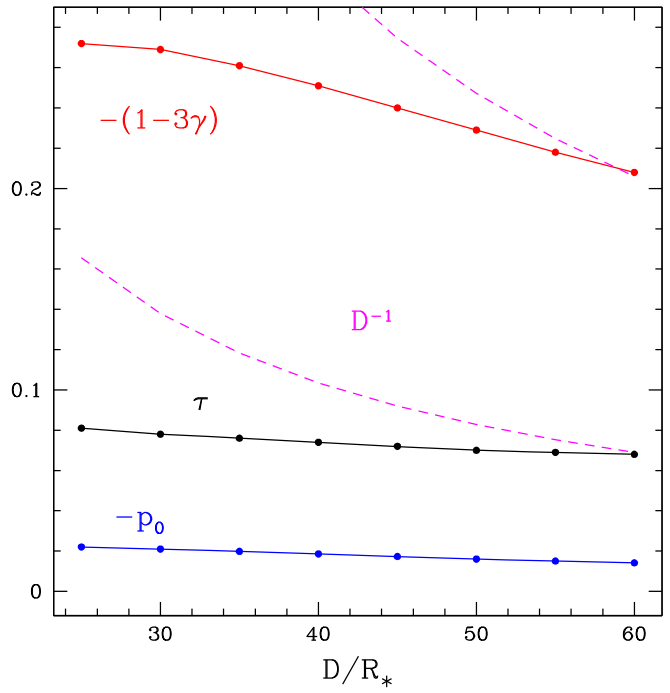

Figure 5. For the case of two equal stars and a planar shock, $\tau = \tau_1 = \tau_2$ and $\gamma = \gamma_1 = \gamma_2$. The figure shows the variations of these parameters along with $p_{\rm tot}$ as a function of binary separation, D/R_*, where $R_* = R_1 = R_2$. Example lines of D^{-1} variation are shown for reference; the parameters determining the colliding-wind polarization decline much more slowly than D^{-1}. Note that since $p_{\rm tot} < 0$, its negative is plotted for convenience.

secondary and intercepting the primary. When the case is reversed, all the subscripts are reversed. This allows us to find δ from the definition above, and the radial integration along the ray segment is δ.

The columns now become

$$\langle N_{C1,III} \rangle = \frac{1}{2} n_{2,0} R_{2,*} \frac{R_{2,*}}{D} \int_0^{\theta_{2,*}} \delta(\theta_1) d\theta_1, \quad (50)$$

$$\langle N_{C2,III} \rangle = \frac{1}{2} n_{1,0} R_{1,*} \frac{R_{1,*}}{D} \int_0^{\theta_{1,*}} \delta(\theta_2) d\theta_2, \quad (51)$$

$$\langle \tilde{N}_{C1,III} \rangle = \frac{1}{2} n_{2,0} R_{2,*} \frac{R_{2,*}}{D} \int_0^{\theta_{2,*}} \delta(\theta_1) \cos^2\theta_1 \, d\theta_1, \quad (52)$$

$$\langle \tilde{N}_{C2,III} \rangle = \frac{1}{2} n_{1,0} R_{1,*} \frac{R_{1,*}}{D} \int_0^{\theta_{1,*}} \delta(\theta_2) \cos^2\theta_2 \, d\theta_2. \quad (53)$$

3.2. Special Case of a Planar Shock

For a binary consisting of two identical stars, $\alpha = \beta = 1$, and the resulting CWI is a planar shock located midway between the stars at $D/2$ from either one. The Appendix details the simplifications that result for this scenario, in particular an analytic expression for $R_{S,1} = R_{S,2}$ in terms of μ, $K_1 = K_2$, and the surface density distribution.

We introduce the simplifying notation $\tau = \tau_1 = \tau_2$ and $\gamma = \gamma_1 = \gamma_2$ and display in Figure 5 how these properties vary with separation between the stars. Note also that $p_1 = p_2 \equiv p_0$, and because the two stars have $L_1 = L_2$, p_0 is a constant at all wavelengths. For this figure we assume a stellar radius of $10R_*$, wind speed 2000 km s^{-1}, and mass-loss rates $10^{-5}\,M_\odot$ yr^{-1}. The polarization amplitude scales with $\dot{M}/v$ for the case of equal stars.

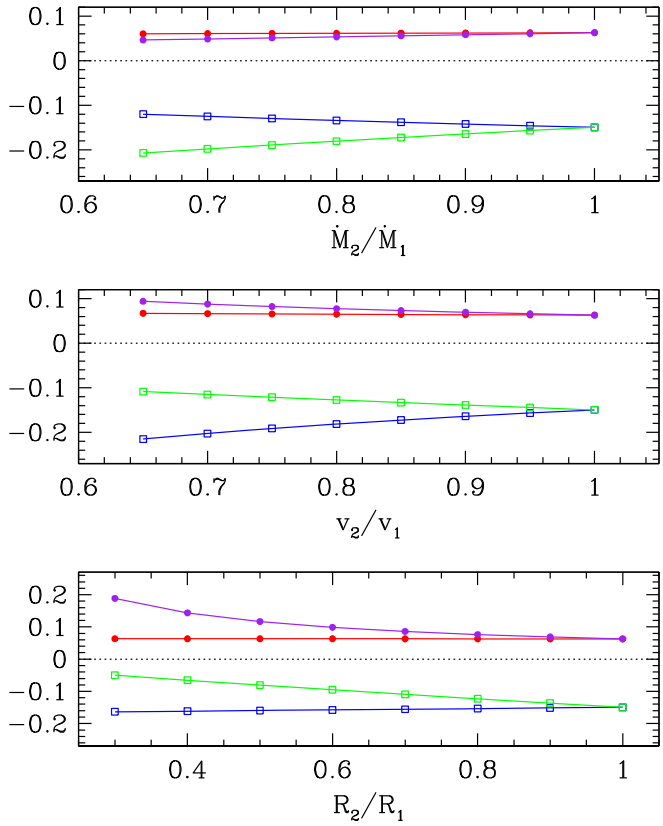

Figure 6. Variation of optical depth τ_1 (red) and τ_2 (purple) and shape factors $(1 - 3\gamma_1)$ (blue) and $(1 - 3\gamma_2)$ (green) for the parameter study with model properties detailed in Table 1; filled points are optical depths, and open squares are for the shape factors involving γ. The top panel shows how the polarization varies with the ratio of mass-loss rates for the stars; the middle panel is for the ratio of wind speeds, $v_2/v_1 = \alpha$; the bottom panel is for the ratio of stellar radii. For each panel, the eight points on the curves correspond to model calculations for the eight parameter combinations shown in Table 1.

By our convention for Figure 1, both $(1 - 3\gamma)$ and p_0 are negative, so they are shown in Figure 5 as multiplied by -1 for convenience. Since many, but not all, terms associated with the calculation scale as D^{-1}, dotted magenta curves are shown with that scaling for comparison. The outcome is that the polarization amplitude p_0 does indeed decline with binary separation, but much less steeply than D^{-1}; its behavior is closer to linear for the chosen parameters and distances shown.

3.3. Parameter Study

We conducted a parameter study of relatively similar winds for primary and secondary components. Results are displayed in Figure 6, with model parameters identified in Table 1. The figure has three panels with model parameters similarly grouped in Table 1. The top is for variation of the ratio of mass-loss rates (which turns out to be β because α is fixed), the middle is for variation of the ratio of the wind terminal speeds (which is $\alpha = v_2/v_1$, but also $\beta = \alpha$ for fixed mass-loss rates), and the bottom is for variation of radii. Note that for the top and middle panels the far right side corresponds to equal winds and a planar shock. For the bottom panel, $\beta = 1$ and the shock is always planar.

In the top panel, the ratio of mass-loss rates varies from 0.65 up to 1.0. The four curves are for τ_1 in red, τ_2 in purple, $1 - 3\gamma_1$ in blue, and $1 - 3\gamma_2$ in green. While the primary wind has the higher optical depth, the deviation of the envelope from

Table 1
Stellar and Wind Properties for the Parameter Study Displayed in Figure 6

Panel	$R_{2,*}$ ($R_\odot$)	$R_{1,*}$ ($R_\odot$)	$\dot{M}_2$ ($10^{-7}\,M_\odot\,\mathrm{yr}^{-1}$)	$\dot{M}_1$ ($10^{-7}\,M_\odot\,\mathrm{yr}^{-1}$)	v_2 ($10^3\,\mathrm{km\,s}^{-1}$)	v_1 ($10^3\,\mathrm{km\,s}^{-1}$)	D ($R_\odot$)
Top	10	10	65	100	2	2	100
Top	10	10	70	100	2	2	100
Top	10	10	75	100	2	2	100
Top	10	10	80	100	2	2	100
Top	10	10	85	100	2	2	100
Top	10	10	90	100	2	2	100
Top	10	10	95	100	2	2	100
Top	10	10	100	100	2	2	100
Middle	10	10	100	100	1.3	2	100
Middle	10	10	100	100	1.4	2	100
Middle	10	10	100	100	1.5	2	100
Middle	10	10	100	100	1.6	2	100
Middle	10	10	100	100	1.7	2	100
Middle	10	10	100	100	1.8	2	100
Middle	10	10	100	100	1.9	2	100
Middle	10	10	100	100	2.0	2	100
Bottom	3	10	100	100	2	2	100
Bottom	4	10	100	100	2	2	100
Bottom	5	10	100	100	2	2	100
Bottom	6	10	100	100	2	2	100
Bottom	7	10	100	100	2	2	100
Bottom	8	10	100	100	2	2	100
Bottom	9	10	100	100	2	2	100
Bottom	10	10	100	100	2	2	100

spherical increases faster for the secondary (green) than the primary (blue) as β declines. This is an important feature of the discussion in Section 3.6, where small β values are emphasized as being typical of WR+OB binary systems.

For the middle panel, $\beta = \alpha$, yet the behavior is reversed. Lowering the wind speed of the secondary actually elevates the density scale for its wind.

Finally, for the bottom panel, $\beta = \alpha = 1$ is fixed, and the wind shock is planar. Despite the geometry being invariant, the polarization depends on the radii of the two stars. This arises because the polarization properties scale with column density, which are generally inverse to radius. For example, with a secondary smaller than the primary yet having the same mass-loss rate and wind speed, the column density is higher in the secondary wind, so τ_2 (purple) increases with decreasing R_2.

3.4. Chromatic Effects

To illustrate chromatic effects, we fixed a particular set of binary parameters while allowing the temperatures of the two stars to vary. The fixed properties lead to $p_1 = 0.009$ and $p_2 = 0.192$. In this example, the binary components are separated by $40\,R_\odot$. The secondary is twice as large ($10\,R_\odot$) as the primary ($5\,R_\odot$), the two winds have equal speeds ($2000\,\mathrm{km\,s}^{-1}$), and the mass-loss rate for the primary is $3.3\times$ larger than the secondary ($\dot{M}_2 = 3\times10^{-6}\,M_\odot\ \mathrm{yr}^{-1}$). Additionally, we took $\sin i = 1$; the effect of viewing inclination is to scale the curves by $\sin^2 i$ at all wavelengths.

To illustrate changes in the spectropolarimetric continuum shape, we treated the two stars as simple Planckian sources with effective temperatures T_1 and T_2. We fixed the temperature of the secondary at $T_2 = 25{,}000$ K. We varied the temperature of the primary from 16,000 to 40,000 K in 3000 K intervals, and we display the results in Figure 7, where polarization is shown as positive. These variations may not be consistent with actual combinations of parameters for real stars. The point of the exercise is to highlight the fact that when the stars have different SEDs, the continuum polarization is not generally constant with wavelength, even though electron scattering is gray. Only when the two stars have equal

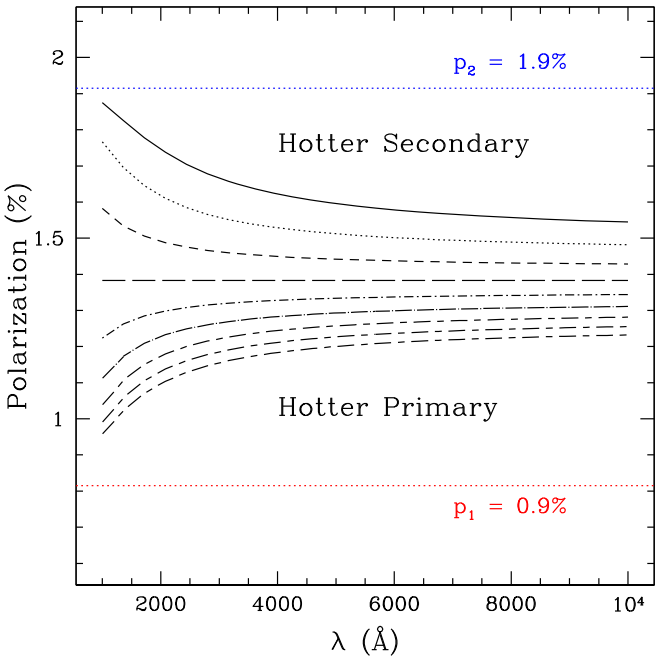

Figure 7. Variation of the polarized continuum with wavelength, here shown from the FUV to 1 μm. The stars are treated as Planckian. The temperature of the secondary is fixed at 25,000 K, and the temperature of the primary varies from 16,000 to 40,000 K in 3000 K increments. The particulars of the stellar and wind parameters for this illustrative case are described in Section 3.4. For the selected parameters, the limiting polarizations p_1 and p_2 are indicated with horizontal red and blue dotted lines, respectively.

temperatures is the continuum polarization truly flat at all wavelengths.

Note especially that the polarization signal changes strongly from the far-UV (FUV) through the optical to 1 μm. For massive stars with typical temperatures well in excess of 10,000 K, both the primary and secondary spectra are in the Rayleigh–Jeans tail in the optical, and so the continuum will always be flat or nearly flat in that wave band. It is only in the UV that the polarization deviates significantly from constant. For the selected parameters, the polarization actually drops toward the UV when the primary is hotter (i.e., more luminous), due to the fact that $p_1 \ll p_2$. By contrast, when the secondary is hotter (i.e., more luminous), the polarization increases significantly. Ultimately, for any combination of binary parameters, when the more luminous star in the UV also has the higher polarimetric component (i.e., p_1 or p_2), the polarization is enhanced in the UV relative to the optical; when the more luminous UV source has the lower polarimetric component, the polarization will drop toward the UV.

The behavior in Figure 7 is included in the formalism of BME but is specific to binaries with two hot stars. Other categories of binaries can certainly show rather different behavior. For example, consider symbiotic stars, which involve a hot white dwarf and a cool giant star (e.g., Muerset et al. 1991). In such a case, the polarigenic opacity may be more complex than simple electron scattering (i.e., not simply gray opacity) and may not involve a colliding wind but perhaps instead accretion onto a disk. Nonetheless, if the scattering opacity is dominated by Thomson scattering, the combination of an optically bright component with a UV-bright component would yield a wavelength-dependent polarization that would reveal a telltale gradual variation from the FUV to the IR.

In any situation where intrinsic polarization from Thomson scattering is observable over a wide spectral domain (separable from interstellar polarization by its binary variation in the time domain, or line effects in the stellar winds, or modeling the wavelength dependence of the interstellar polarization), these results show that the residual wavelength dependence of the intrinsic polarization offers a unique and important diagnostic. Via the following analysis, we obtain complementary leverage in our understanding of both the different polarizations produced by the two stellar light sources and the spectral shape of the continua of both stars. This stems from the grayness of Thomson scattering, which implies that the sole source of wavelength dependence in the intrinsic polarization derives from the contrasting brightnesses of the two stars. Hence, if $L_{21}(\lambda)$ is the wavelength-dependent ratio of the secondary brightness to the primary, then the total polarization $q(\lambda)$ presents as a brightness-weighted average of the wavelength-independent polarization induced by the primary light source, q_1, and that induced by the secondary, q_2, according to

$$q(\lambda) = \frac{q_1 + q_2 L_{21}(\lambda)}{1 + L_{21}(\lambda)}. \tag{54}$$

If the spectral shape contrast $L_{21}(\lambda)$ is regarded as known by the stellar spectral types, then observing q at two different wavelengths that sample suitably different values of $L_{21}(\lambda)$ allows the above equation to separate the q_1 and q_2 contributions. This separation of the polarizations caused by the two different light sources allows a unique probe of the geometry of the wind collision zone.

Furthermore, to the extent that q_1 and q_2 are expected to be wavelength independent, a self-consistency check on the assumed $L_{21}(\lambda)$ becomes possible by inverting the above equation into

$$L_{21}(\lambda) = \frac{q_1 - q(\lambda)}{q(\lambda) - q_2}. \tag{55}$$

To whatever extent this inferred brightness contrast deviates from its assumed value, we have the opportunity to update it to recover consistency with the polarized spectrum $q(\lambda)$. For example, a (q_1, q_2) pair can be inferred from wavelength pairs generated by fixing a wavelength at the UV end of the observed $q(\lambda)$ and sweeping the second wavelength over the full observed range. If the assumed $L_{21}(\lambda)$ contains errors, that would generate a curve in (q_1, q_2) space rather than a single consistent point. Then, by fixing the second wavelength at its longest value and sweeping the first wavelength back toward the UV, the curve is closed back to its starting (q_1, q_2) point. The resulting closed curve then gives an estimate of the preferred (q_1, q_2) value near the center of this curve, and that preferred (q_1, q_2) pair then allows $L_{21}(\lambda)$ to be self-consistently updated via the above equation. The wavelength independence of the intrinsic polarization contributions q_1 and q_2, assuming that they are dominated by Thomson scattering in the colliding winds, then provides an improved estimate of $L_{21}(\lambda)$ and an independent check of our understanding of binary spectral types. In addition, when both q_1 and q_2 are appreciable, independent knowledge of both allows an important probe of the colliding-wind geometry, since the two stars illuminate that geometry differently.

On the other hand, in situations where one contribution dominates, say, q_1, as may be the case in WR/O binaries discussed below, the wavelength dependence of the intrinsic $q(\lambda)$ directly inherits the wavelength dependence of $L_{21}(\lambda)$ via $q(\lambda) = q_1/(1 + L_{21}(\lambda))$. Hence, in this case we have an even more direct handle on the correct brightness contrast between the two stars over the full wavelength regime of the observed polarization. The wider that wavelength regime accessed by our technology, the more powerful is this constraint, underscoring the value of extending our polarization capabilities into the FUV range for understanding binaries containing hot stars.

3.5. Orbital Effects

The polarimetric properties of the colliding-wind system depend on the binary separation, D. When the orbit is circular (i.e., D is constant), the values p_1 and p_2 are constant as well. For an eccentric orbit with eccentricity e and semimajor axis a, the binary separation varies as

$$D(\varphi) = a\,\frac{1 - e^2}{1 + e\cos\varphi}, \tag{56}$$

where φ is the orbital azimuth, defined so that $\varphi = 0$ corresponds to periastron. Thus, p_1 and p_2 are functions of orbital phase through the variation of $D(\varphi)$.

The polarization also varies throughout the orbital motion because the inclination, i, of the LOC between the stars changes relative to the observer's line of sight. Let $i_{\rm orb}$ be the viewing inclination of the orbital plane, so that $i_{\rm orb} = 0^\circ$ is a top-down view of the orbit and $i_{\rm orb} = 90^\circ$ is an edge-on view.

Despite a fixed orientation of the orbital plane, $i_{\rm orb}$, our construction for calculating polarization depends on the system axis defined by the LOC between the stars, and this rotates in the fixed orbital plane to produce variability.

The time-variable polarization is given by

$$q = p_0(D)\sin^2 i(t)\cos 2\psi(t), \tag{57}$$

$$u = p_0(D)\sin^2 i(t)\sin 2\psi(t), \tag{58}$$

where $D = D(t)$ for eccentric orbits, t depends on orbital phase through the azimuth (φ of the LOC), and the polarization position angle ψ relates to the orbital azimuth and the fixed viewing inclination of the orbital plane via

$$\tan\psi = -\cos i_{\rm orb} / \tan\varphi. \tag{59}$$

The inclination, i, for the LOC to the viewer's line of sight is given by

$$\cos i = \sin i_{\rm orb}\cos\varphi. \tag{60}$$

In order to understand the relevance of CWIs for the polarization level, we introduce the idea of "noninteracting winds" (NIWs). The concept of an NIW provides a reference against which to compare the physical case of CWI polarization arising from the shock. What CWI ultimately represents is a redistribution of matter from the two stellar winds via the wind collision. There is polarization without a CWI because each of the two stars shines on the wind of the other, even if both winds remain spherical. The CWI represents another contribution by breaking spherical symmetry. For wide binary separations ($D \gg R_*$), we expect the two cases to become proportional, since the column depths of the various regions will scale as D^{-1} (see the Appendix).

We thus define an NIW simply as a superposition of the two separate binary winds as if no collision takes place and neither wind impacts the opposite star. This means that each wind is spherically symmetric about its own star, which contributes no polarization. Instead, polarization arises only from scattering of starlight from the secondary by the wind of the primary, and vice versa. We do, however, account for occultation of the wind behind each respective star in calculating the polarization.

Our results are shown in Figure 8, with the polarization amplitude in percent for the NIW along the horizontal and for the CWI along the vertical. For this example we assume two equal winds and thus a planar shock for the CWI case. The points represent stellar separations of $D = 25{-}115\,R_\odot$ in $5\,R_\odot$ increments, with closer and farther separations labeled for the sequence. The values are for a face-on binary, oriented so that $u = 0$ and $q < 0$, and $p = |q|$ for this plot. The dotted diagonal indicates where the polarizations would be equal; the solid green line is the asymptotic relation derived in the Appendix.

For the CWI case, we fitted a linear regression to $p_0(D)$ in the case of a binary with two identical stars (i.e., planar CWI shock) to obtain $p_0 = 1.328 - 0.0111D$, normalized so that $p_0 = 1\%$ at $D = 30\,R_\odot$. For the NIWs, we used the same stellar wind and star properties as for the wind collision case. The polarization from a CWI is larger than for an NIW, often by a significant factor. At larger separations, the trend is for the points to approach the diagonal line, signifying that the wind collision is becoming irrelevant.

We recognize that we are using a model for a bow shock with radiative cooling and that at large separations the cooling will be adiabatic. Even so, with identical stars and winds, the shock will still be planar, and the qualitative conclusion remains valid even if the quantitative values are inaccurate.

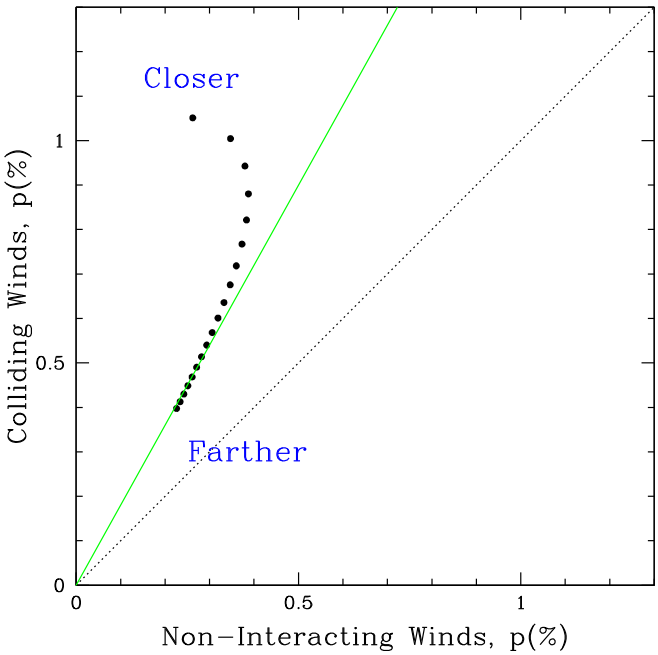

Figure 8. Comparison of the percent polarization from a face-on binary system with colliding winds against that from a binary with NIWs (Section 3.5). The points represent separations of $25{-}115\,R_\odot$ in $5\,R_\odot$ increments, with monotonic sequence as indicated by "Closer" and "Farther." Wind collision significantly increases the level of polarization of colliding winds over NIWs, but less so as the binary separation increases to large values. The green line represents the analytic derivation from the Appendix for wide binary separations.

Figure 9 displays a suite of polarimetric variations for CWIs with different values of e and $i_{\rm orb}$. We show model variable polarization curves for inclinations and eccentricities, as labeled. The top panel displays the resulting $q - u$ loops; the bottom panel shows polarized light curves as a function of orbital phase. At $i_{\rm orb} = 90°$ (not shown), all curves in Figure 9 would become horizontal lines with only q variation but no u variation. Note also that $p_{\rm tot} = \sqrt{q^2 + u^2}$.

3.6. Special Case of WR+OB Binaries

Among the more extreme massive-star colliding-wind systems ($\beta \ll 1$) are the ones involving an evolved WR star with an OB companion. While the wind speeds of the two stars can be comparable in this case, the mass-loss rate of the WR wind will be one to several orders of magnitude larger than for the OB component. As a result, the CWI shock is significantly displaced from the WR star and considerably closer to the OB star; it also significantly confines the spatial scope of the OB wind. On the other hand, the WR and OB components may or may not have comparable luminosities. In terms of a UV study, the situation can be ideal for extracting information about the orbital parameters and properties of the CWI region from both temporal and chromatic effects.

The scenario of $\beta \ll 1$ offers some simplifications for the problem of the polarization. Foremost is that the "primary" (defined as above as the WR wind with higher mass loss, not necessarily the more luminous component) is relatively far from the CWI shock. Consequently, one expects the angle-averaged column densities over the WR wind component to approach zero. The associated column densities for the

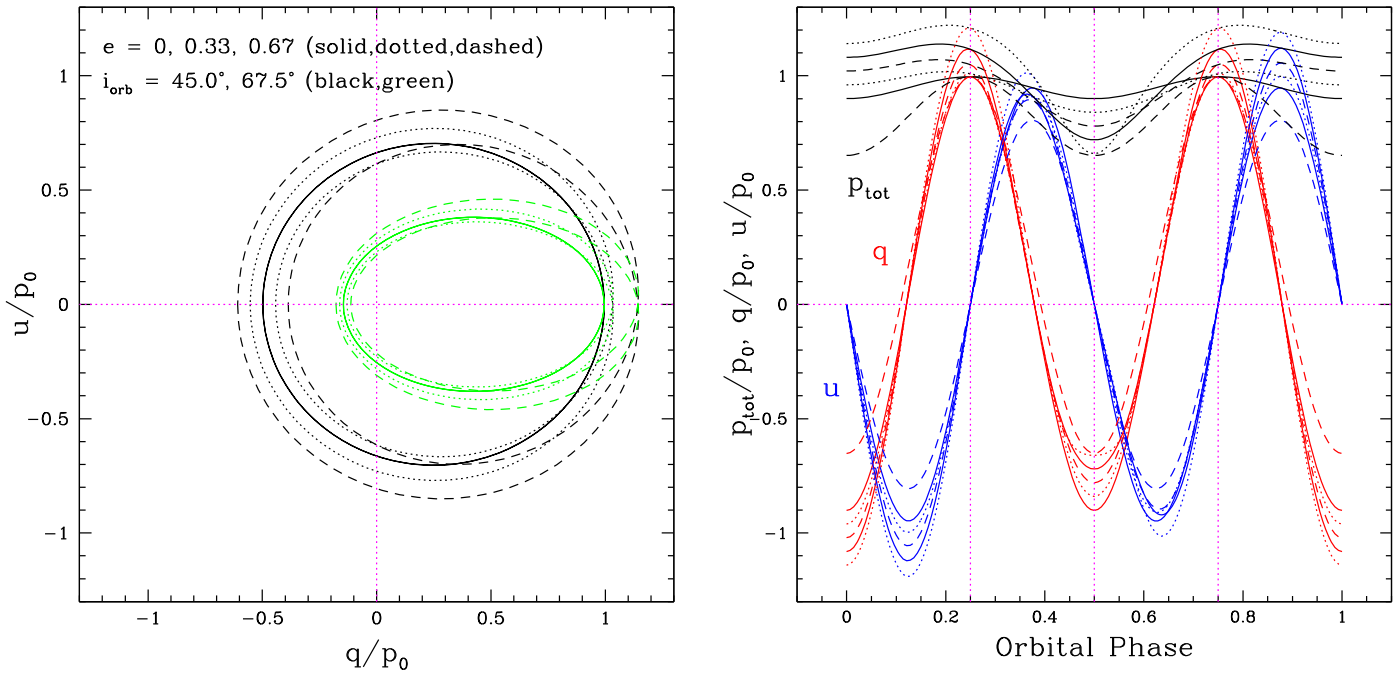

Figure 9. Top: example $q-u$ loops for a binary consisting of identical stars, for which $p_1 = p_2 \equiv p_0$. Eccentricities e and inclinations $i_{\rm orb}$ are indicated for line type and color. There are two loops per orbit, but with eccentric orbits, the pair separate into different sizes except for $e = 0$. Bottom: same six models as in the top panel, but now displayed as light curves in q (red), u (blue), and total polarization $p_{\rm tot}$ (black). Periastron passage is at phase 0.0, and apastron at phase 0.5. The line types still relate to e as in the top panel. The case $i_{\rm orb} = 45°$ has the higher polarization in $p_{\rm tot}$ and larger amplitude variation in q and u.

secondary wind evaluated at the primary will be small. It may seem that $p_1 = p_{\rm WR}$ would be dominated by the CWI shock, but this may not mean that the WR component dominates the polarization, since the CWI is relatively far removed and thus only acts as a perturbation on the otherwise spherical wind of the WR star. The result for the O star, $p_2 = p_{\rm O}$, is less clear. Its wind has lower column density than the WR, but the distorted envelope is closer to the O star at low β. In addition, the CWI wraps around the O star, leading to polarimetric cancellation. We use the Cantó et al. (1996) formalism to evaluate the possibilities.

To illustrate some of these features, Figure 10 shows a density contour plot in the orbital plane for a WR+OB binary. The WR star is the smaller star at right; the secondary is taken to be an O star. The dotted curves are density contours at approximately 0.5 dex intervals, with two labeled for illustration, normalized to unit density at the surface of the WR star.

To explore the polarization expected from WR+OB colliding winds, we adopted the following stellar and orbital parameters. For the WR as primary and an O star as secondary, we assumed $M_1 = M_2 = 30\ M_\odot, R_1 = R_\odot,\ R_2 = 12\,R_\odot$, and $v_1 = v_2$ so that $\alpha = 1$, and we considered orbital scenarios ranging from a short-period orbit of $P_S = 7$ days to a medium-period orbit of $P_M = 30$ days (a typical range for colliding winds in circular orbits; see, e.g., Fahed & Moffat 2012; Zhekov 2012). Given the masses, these two orbits correspond to semimajor axes of $a_S = 60\,R_\odot$ and $a_M = 160\,R_\odot$.

As a fiducial, we also adopted $\dot{M}_1 = 10\ \dot{M}_2$ so that $\beta = 0.1$. At this value of β, the relative standoff distance for the bow shock is $R_{S,2}/D = 0.24$, which is a fixed ratio regardless of binary eccentricity, given that we assumed that the winds are at terminal speed. For the short-period binary, we assumed a circular orbit, hence $R_{S,2} = 14.4\,R_\odot$. For a typical O star wind, this would be well within the zone of wind acceleration, where

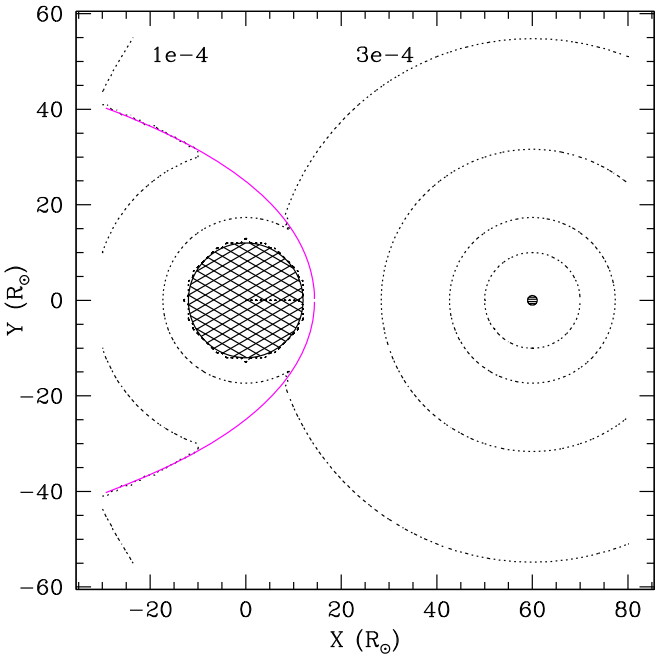

Figure 10. Top-down view of a WR+OB binary with density contours superposed. The WR star is the smaller component at right; at left is the OB star. The magenta curve highlights the CWI shock. Two representative contours indicate relative densities, normalized to unity at the surface of the WR star. The contours are displayed in roughly 0.5 dex intervals. In this example, the binary separation is 60 $R_\odot$, the OB star has a radius of 12 $R_\odot$, and the WR star has a radius of 1 $R_\odot$.

effects such as radiative braking could be significant (as seen in the WR+O binary V444 Cyg; Lomax et al. 2015). For the sake of illustration, we ignored such effects.

We calculated $p_{\rm WR}$ and $p_{\rm O}$ for three scenarios, with a summary of results displayed in Figure 11. The first case is

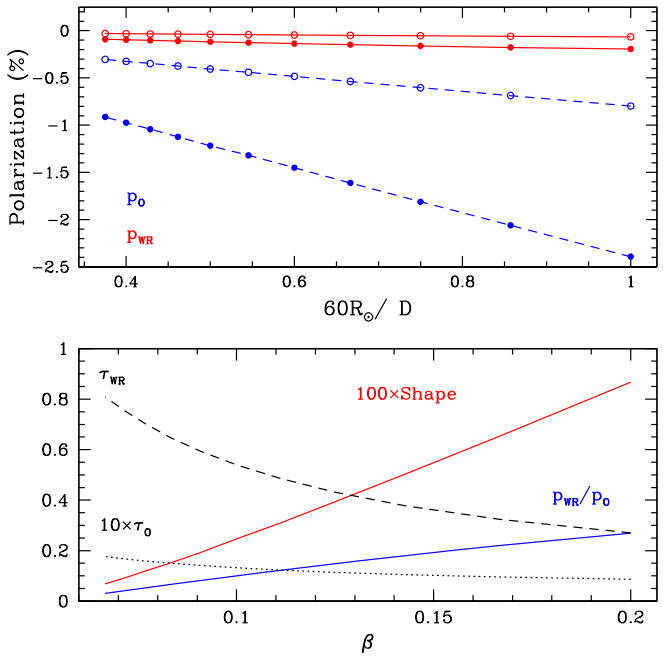

Figure 11. Model results for a WR+O star binary (Section 3.6). The top panel shows results for a fixed value of $\beta = 0.1$ for the slow and fast wind cases, plotted against binary separation as D^{-1}. Blue lines represent $p_{\rm O}$, and red lines represent $p_{\rm WR}$; solid circles are for slow models and open circles for fast wind models. The bottom panel shows results for $D = 160\,R_\odot$ with β varying between $1/15$ and $1/5$. Black curves represent the WR and O optical depths, as labeled. The blue line in this panel represents the ratio of $p_{\rm WR}/p_{\rm O}$. The red line represents the "shape," defined as the ratio $(1 - 3\gamma_{\rm O})/(1 - 3\gamma_{\rm WR})$ and scaled up by 100 times.

$\beta = 0.1$ with orbital separation ranging from 60 to 160 $R_\odot$ for "slow" winds of 1000 km s^{-1} for both stars. The second case is for fast winds at 3000 km s^{-1}, with all other parameters fixed. The third scenario corresponds to an intermediate wind speed of 2000 km s^{-1} at a fixed separation of $D = 160\,R_\odot$, but with β ranging between $1/15$ and $1/5$.

The top panel of Figure 11 summarizes the comparison between slow and fast winds. Note that polarization is negative for our convention. In this panel, the red lines represent $p_{\rm O}$ and the blue lines represent $p_{\rm WR}$. The solid circles are for the slow-wind cases, and the open circles are for the fast-wind cases. The results are plotted against D^{-1}, normalized as indicated. The net result is that the polarization is overall larger for a slower wind, since the density is larger. We find that $\tau_{\rm WR}$ is roughly constant as D changes, indicating that its value is dominated by the relatively extended spherical wind of the WR star, since the CWI is far removed. Because the CWI is relatively farther from the WR star with increasing D, $(1 - 3\gamma_{\rm WR})$ becomes smaller with D. Consequently, $p_{\rm WR}$ decreases with increasing D. The behavior for the O star is that the polarization is dominated by the CWI. The surface density of the CWI shock for the Cantó et al. (1996) solution scales as D^{-1} overall. This is evidenced by the fact that both blue curves appear quite linear in the plot.

For the bottom panel of Figure 11, we display the results differently, as β is allowed to vary between $1/15$ and $1/5$; with smaller β, the CWI is closer to the O star component. Consider first the dashed and dotted curves in black, for $\tau_{\rm WR}$ and $\tau_{\rm O}$, respectively. As β becomes smaller, $\tau_{\rm WR}$ is larger, approaching the limit of the strictly spherical wind value. The value of $\tau_{\rm O}$ is much lower and is plotted as scaled up by 10 times.

The blue curve in the bottom panel represents the ratio of $p_{\rm WR}/p_{\rm O}$. Its behavior indicates that from geometrical considerations the contribution to the polarization from the O star wind is much greater than for the WR wind, even more so as β becomes smaller. Even though the WR wind has a much higher optical depth scale, the distortion of the scattering envelope from spherical is quite minor from the perspective of the WR star. This is made clear by the red curve, where "shape" is the ratio $(1 - 3\gamma_{\rm WR})/(1 - 3\gamma_{\rm O})$ and scaled up by 100 times. From the perspective of the O component, the scattering envelope is highly distorted.

In combination, these results suggest that at wavelengths where the O star is more luminous, the polarization will overall be larger (biased toward $p_{\rm O}$) than at wavelengths where the WR star is more luminous (polarization biased toward $p_{\rm WR}$). Our treatment does have limitations, the most important being that we ignore the wind acceleration region and that we treat the WR wind as optically thin to electron scattering. Radiative transfer models have shown that multiple scattering in bow shock structures can increase the degree of polarization, as well as changing the polarization behavior with inclination angle (Shrestha et al. 2018). However, in this case it is clear that the WR wind is already a minor contributor to the polarization when $\beta \ll 1$, and a more full treatment of multiple scattering at the inner WR wind is not expected to impact that conclusion. For the rare case of WR–WR binaries, multiple scattering could be significant, and future modeling will need to take it into consideration. Inclusion of the wind acceleration region and associated density distribution, along with radiative inhibition, could certainly change the detailed outcomes of the models presented here. Additionally, WR+O binaries can generally be expected to show chromatic behavior over a broader wave band than indicated in Section 3.4. Free–free opacity is important in the winds of WR stars at all wavelengths; hence, the WR stellar spectrum is never Rayleigh–Taylor even though the OB SED can be (e.g., Hillier 1987). Nonetheless, the present treatment indicates that $p_{\rm O} \gg p_{\rm WR}$, another qualitative result that is unlikely to change despite our more simplistic assumptions.

3.7. Comment on the Overall Scale of the Polarization

As mentioned above for identical stars, the polarization is proportional to $\dot{M}/v$. This extends more generally to unequal stars, where the two different mass-loss rates receive different weightings, as a change in both mass-loss rates by any given factor produces a change in polarization by that same factor. This implies that a good model of the polarizing geometry allows the scale of the observed polarization to yield a constraint on the stellar mass-loss rates that is independent, and hence complementary, of all other methods for such determinations. Furthermore, to the extent that the polarization is due to optically thin scattering, the connection between polarization and mass-loss rate is independent of local clumping in the winds. Hence, contrasting the mass-loss rates inferred from the overall scale of the polarization to those obtained from conventional methods that are sensitive to clumping (often termed "density-squared"-type mass-loss rate diagnostics such as radio free–free emission or Hα emission) provides an independent measure of the degree of clumping. Constraining wind clumping is an important goal for understanding the basic dynamics of radiatively driven winds.

4. Summary

This study has made use of the theory of BME for optically thin electron scattering polarization for a massive colliding-wind binary. The main novelty has been to explore the analytic solution for the CWI shock structure in terms of shape and density from Cantó et al. (1996), who assume radiative cooling to derive a thin-shell result. We assume axisymmetry throughout and explore polarization characteristics and contributions from the two separate components. Our results range from the limiting case of equal star scenarios with $\beta = 1$ and a planar shock interface (more appropriate to O+O binaries) to small β scenarios (more appropriate to WR+O binaries).

Overall, there are numerous free parameters for the model, from the binary separation to the wind properties. Even when most star and wind properties are held fixed, raising and lowering the terminal wind speeds at fixed ratio α still affects the polarization characteristics, since slower winds are denser and faster ones are less dense.

Our three main results are as follows:

1. From a detailed consideration of the contributions to the column density moments, there are various terms that scale with D^{-1} for the binary separation. However, for the equal wind scenario, the scale of polarization declines far less steeply than D^{-1}, so that even relatively wide binaries may display a significant polarimetric amplitude, with a telltale orbitally varying phase angle. (See Figure 5.)
2. Chromatic effects can become quite significant toward UV wavelengths. When dealing with massive stars, all of which are "hot" at $> 10{,}000$ K, the optical emission is mostly or even very closely following the Rayleigh–Jeans law. The consequence is that for optical and longer wavelengths the continuum polarization is flat. That polarization can still vary with orbital phase, but there are no chromatic effects. However, at UV wavelengths for stars with different temperatures, the continuum polarization will generally deviate from flat (unless one star dominates the luminosity at all wavelengths). The wavelength-dependent polarization provides additional diagnostic leverage for extracting information about the winds and CWI shock (Figure 7). This motivates UV polarimetric observations of colliding-wind binaries, such as would be provided by the proposed Polstar satellite (Scowen et al. 2021).
3. Orbital effects produce distinguishable shapes in the q–u plane. The shapes are mainly elliptical, as pointed out by BME already. Importantly, we used the context of orbital effects to explore the influence of the CWI shock, and its boundary separating the two stellar winds, on the amplitude of polarization. For this purpose we introduced the NIW construct. This assumes an (unphysical) superposition of the respective two winds, with polarization arising solely from each star shining on the spherical wind of the other. In this way the scenario for NIWs and CWIs can be compared on the scale of the same mass fluxes. For the case of equal winds and a planar shock, inclusion of the CWI increases the polarization by factors of several, until the separation of the two stars becomes large compared to the stellar radii. As expected, the CWI and NIW polarizations become equal, since the CWI is far removed from either star and thus adds only a small column density compared to the spherical winds.
4. When $\beta \ll 1$, as, for example, in the case of WR+OB binaries, we find the interesting result that the polarization for the OB component is much higher than for the WR component. Whether the observed polarization is dominated by the WR or the OB star will depend on the weighting by the specific luminosities. However, it is clear that at wavelengths where the WR star is more luminous, the polarization will be lower as set by $p_{\rm WR}$, and where it is less luminous, the polarization will be higher as set by $p_{\rm O}$ (or $p_{\rm B}$, as the case may be; Figure 11.)

In closing, it is worth noting that the individual stars in a massive colliding-wind system may themselves be sources of polarization, which may be steady or variable. For example, around 10% of massive stars are known to be magnetic (Wade et al. 2016), and it is possible (although very rare) for massive-star binaries to have a component that possesses a significant magnetic field (e.g., Plaskett's star; Grunhut et al. 2013). Munoz et al. (2022) have recently explored the effects of variable linear polarization from electron scattering for rotating magnetospheres. While this could complicate efforts to isolate the variable polarization from the CWI, the polarization from individual stars will be modulated on a rotation period, whereas the colliding-wind polarization is modulated on the orbital period. Unless the binaries are very close, these periods are unlikely to be the same.

WR stars in particular are known to be sources of polarization. However, typical polarization behavior from individual WR stars appears stochastic (e.g., St.-Louis et al. 1987; Drissen et al. 1987). The behavior is likely associated with the wind flow time, R_*/v_∞, which is much shorter than binary orbital periods. In addition to being stochastic in nature, the effect could be averaged out to emphasize the smoother variable polarization from the CWI on the longer period of the orbit. In addition to variable polarization, some WR stars may have long-term stable polarizations (e.g., Harries et al. 1998). Abdellaoui et al. (2022) have explored the polarization that could result for axisymmetric rotationally distorted winds of WR stars. However, such polarization would be constant. The effect would be to contribute to a constant offset to the system polarization, similar to the effect of interstellar polarization. Variable polarization would arise entirely from the CWI over the timescale of the orbital period.

R.I. acknowledges funding support for this research from grants by the National Science Foundation (NSF), AST-2009412 and AST-1747658. Y.N. acknowledges support from the Fonds National de la Recherche Scientifique (Belgium), the European Space Agency (ESA), and the Belgian Federal Science Policy Office (BELSPO) in the framework of the PRODEX Programme. J.L.H. is grateful for NSF funding under award AST-1816944 and acknowledges that the University of Denver occupies land within the traditional territories of the Arapaho, Cheyenne, and Ute peoples. N.S.L. wishes to thank the National Sciences and Engineering Council (NSERC) for financial support.

Appendix
Special Case of $\alpha = \beta = 1$

When $\beta = 1$ and $\alpha = 1$, with stars of identical stellar and wind parameters, the CWI is planar, and the solution for the shock properties simplifies considerably. First, we introduce $\theta = \theta_1 = \theta_2$ as the angle from either star to a point on the planar shock. The distance of the shock from either star becomes

$$R_S = D/2\mu. \tag{A1}$$

The projection factors become $K = K_1 = K_2 = \mu$. Simplification of the surface density was noted already in Equation (16). Contributions to the polarization from the CWI component depend on the following integrals (see Equations (36)–(39)):

$$\int_0^1 \Sigma(\mu) K(\mu) d\mu = 4\Sigma_0$$
$$\int_0^1 \frac{\mu^2(1-\mu)^2}{\sin\theta(\theta - \mu\sin\theta)}\, d\mu \approx 0.56\ \Sigma_0 \tag{A2}$$

and

$$\int_0^1 \Sigma(\mu) K(\mu) \mu^2\, d\mu = 4\Sigma_0$$
$$\int_0^1 \frac{\mu^4(1-\mu)^2}{\sin\theta(\theta - \mu\sin\theta)}\, d\mu \approx 0.32\ \Sigma_0. \tag{A3}$$

Using these two results, we can analytically derive the polarization for the scenario of two equal stars that are widely separated, with $D \gg R_*$. At wide separation we can ignore the finite size of each star (i.e., $\theta_* \to 0$), which amounts to not having to consider case C (see Section 3.1.3). Additionally, the region of case A for each star (see Section 3.1.1) is hemispherical and consequently makes no contribution to the net polarization. All that remains are contributions I, II, and III for case B (see Section 3.1.2), where the limits of the angular integrations are 0 to $\pi/2$ in θ or $+1$ to 0 in μ. The total polarization becomes

$$p = \frac{3}{8}\sigma_T(\overline{N} - 3\widetilde{N}) \tag{A4}$$

$$= \tfrac{3}{8}\sigma_T[\overline{N}_{B,I} + \overline{N}_{B,II} + \overline{N}_{B,III} - 3\widetilde{N}_{B,I} - 3\widetilde{N}_{B,II} - 3\widetilde{N}_{B,III}] \tag{A5}$$

$$= \tfrac{3}{8}\sigma_T\, n_0\, R_*\left(\tfrac{R_*}{D}\right)[-1.00 + 0.56 + 2.47 + 075 - 0.96 - 6.30] \tag{A6}$$

$$= -1.68\ \sigma_T\, n_0\, R_*\left(\frac{R_*}{D}\right), \tag{A7}$$

where each number in the square brackets of Equation (A6) corresponds to each term in the preceding line of Equation (A5). Note that if grouped by region, each of I, II, and III would separately yield net negative polarizations.

For comparison the polarization for the NIW case introduced in Section 3.5 can also be evaluated analytically for $D \gg R_*$. The two relevant angle-averaged column densities are

$$\bar{N} = n_0\, R_*\left(\frac{R_*}{D}\right)\int_0^{\pi/2} \pi\, d\theta = \frac{\pi^2}{2}\, n_0\, R_*\left(\frac{R_*}{D}\right) \tag{A8}$$

and

$$\tilde{N} = n_0\, R_*\left(\frac{R_*}{D}\right)\int_0^{\pi/2} \pi\cos^2\theta\, d\theta = \frac{\pi^2}{4}\, n_0\, R_*\left(\frac{R_*}{D}\right). \tag{A9}$$

For an NIW with wide binary separation, the polarization is

$$p_{\rm NIW} = \tfrac{3}{8}\,\sigma_T\, n_0\, R_*\left(\tfrac{R_*}{D}\right)\left(\tfrac{\pi^2}{2} - 3\tfrac{\pi^2}{4}\right) = -0.93\ \sigma_T\, n_0\, R_*\left(\tfrac{R_*}{D}\right). \tag{A10}$$

The ratio of the coefficients from Equations (A7) and (A10) is 1.8, which is the solid green line appearing in Figure 8.

ORCID iDs

Richard Ignace https://orcid.org/0000-0002-7204-5502
Andrew Fullard https://orcid.org/0000-0001-7343-1678
Yaël Nazé https://orcid.org/0000-0003-4071-9346
Kenneth Gayley https://orcid.org/0000-0001-8742-417X
Jennifer L. Hoffman https://orcid.org/0000-0003-1495-2275
Jamie R. Lomax https://orcid.org/0000-0001-8470-0853
Nicole St-Louis https://orcid.org/0000-0003-3890-3400

References

Abdellaoui, S., Krtička, J., & Kurfürst, P. 2022, A&A, 658, A46
Antokhin, I. I., Owocki, S. P., & Brown, J. C. 2004, ApJ, 611, 434
Brown, J. C., Aspin, C., Simmons, J. F. L., & McLean, I. S. 1982, MNRAS, 198, 787
Brown, J. C., McLean, I. S., & Emslie, A. G. 1978, A&A, 68, 415
Callingham, J. R., Crowther, P. A., Williams, P. M., et al. 2020, MNRAS, 495, 3323
Cantó, J., Raga, A. C., & Wilkin, F. P. 1996, ApJ, 469, 729
Cazorla, C., Nazé, Y., & Rauw, G. 2014, A&A, 561, A92
Drissen, L., St.-Louis, N., Moffat, A. F. J., & Bastien, P. 1987, ApJ, 322, 888
Fahed, R., & Moffat, A. F. J. 2012, MNRAS, 424, 1601
Fahed, R., Moffat, A. F. J., Zorec, J., et al. 2011, MNRAS, 418, 2
Fox, G. K. 1994, ApJ, 432, 262
Gayley, K. G. 2009, ApJ, 703, 89
Gayley, K. G., Owocki, S. P., & Cranmer, S. R. 1997, ApJ, 475, 786
Georgiev, L. N., & Koenigsberger, G. 2004, A&A, 423, 267
Girard, T., & Willson, L. A. 1987, A&A, 183, 247
Gosset, E., & Nazé, Y. 2016, A&A, 590, A113
Gosset, E., Nazé, Y., Sana, H., Rauw, G., & Vreux, J. M. 2009, A&A, 508, 805
Gosset, E., Royer, P., Rauw, G., Manfroid, J., & Vreux, J. M. 2001, MNRAS, 327, 435
Grunhut, J. H., Wade, G. A., Leutenegger, M., et al. 2013, MNRAS, 428, 1686
Harries, T. J., Hillier, D. J., & Howarth, I. D. 1998, MNRAS, 296, 1072
Henley, D. B., Stevens, I. R., & Pittard, J. M. 2003, MNRAS, 346, 773
Hillier, D. J. 1987, ApJS, 63, 947
Ignace, R., Bessey, R., & Price, C. S. 2009, MNRAS, 395, 962
Kallrath, J. 1991, MNRAS, 248, 653
Kennedy, M., Dougherty, S. M., Fink, A., & Williams, P. M. 2010, ApJ, 709, 632
Kurosawa, R., Hillier, D. J., & Pittard, J. M. 2002, A&A, 388, 957
Lamberts, A., Fromang, S., & Dubus, G. 2011, MNRAS, 418, 2618
Langer, N. 2012, ARA&A, 50, 107
Lomax, J. R., Nazé, Y., Hoffman, J. L., et al. 2015, A&A, 573, A43
Luehrs, S. 1997, PASP, 109, 504
MacLeod, M., & Loeb, A. 2020, ApJ, 902, 85
Mossoux, E., & Rauw, G. 2021, A&A, 646, A89
Muerset, U., Nussbaumer, H., Schmid, H. M., & Vogel, M. 1991, A&A, 248, 458
Munoz, M. S., Wade, G. A., Faes, D. M., Carciofi, A. C., & Labadie-Bartz, J. 2022, MNRAS, 511, 3228
Nazé, Y., Koenigsberger, G., Pittard, J. M., et al. 2018, ApJ, 853, 164
Nazé, Y., Mahy, L., Damerdji, Y., et al. 2012, A&A, 546, A37
Nomoto, K., Kobayashi, C., & Tominaga, N. 2013, ARA&A, 51, 457
Parkin, E. R., & Pittard, J. M. 2008, MNRAS, 388, 1047
Pilyugin, N. N., & Usov, V. V. 2007, ApJ, 655, 1002

Puls, J., Vink, J. S., & Najarro, F. 2008, A&ARv, 16, 209
Rauw, G., Mahy, L., Nazé, Y., et al. 2014, A&A, 566, A107
Rauw, G., Mossoux, E., & Nazé, Y. 2016, NewA, 43, 70
Rauw, G., Vreux, J. M., & Bohannan, B. 1999, ApJ, 517, 416
Rodríguez, L. F., Arthur, J., Montes, G., Carrasco-González, C., & Toalá, J. A. 2020, ApJL, 900, L3
Sana, H., de Mink, S. E., de Koter, A., et al. 2012, Sci, 337, 444
Sana, H., Stevens, I. R., Gosset, E., Rauw, G., & Vreux, J. M. 2004, MNRAS, 350, 809
Scowen, P. A., Gayley, K., Neiner, C., et al. 2021, Proc. SPIE, 11819, 1181908
Shrestha, M., Neilson, H. R., Hoffman, J. L., & Ignace, R. 2018, MNRAS, 477, 1365
Shrestha, M., Neilson, H. R., Hoffman, J. L., Ignace, R., & Fullard, A. G. 2021, MNRAS, 500, 4319
Smith, N. 2014, ARA&A, 52, 487
Song, H. F., Meynet, G., Maeder, A., Ekström, S., & Eggenberger, P. 2016, A&A, 585, A120
St.-Louis, N., Drissen, L., Moffat, A. F. J., Bastien, P., & Tapia, S. 1987, ApJ, 322, 870
St.-Louis, N., Moffat, A. F. J., Lapointe, L., et al. 1993, ApJ, 410, 342
Stevens, I. R., Blondin, J. M., & Pollock, A. M. T. 1992, ApJ, 386, 265
Usov, V. V. 1992, ApJ, 389, 635
Wade, G. A., Neiner, C., Alecian, E., et al. 2016, MNRAS, 456, 2
Williams, P. M., Marchenko, S. V., Marston, A. P., et al. 2009, MNRAS, 395, 1749
Zhekov, S. A. 2012, MNRAS, 422, 1332